Kentucky Geological Survey
James C. Cobb, State Geologist and Director
University of Kentucky, Lexington

Source Scaling, Subevent Distributions, and Ground-Motion Simulation in the Composite Source Model

Baoping Shi, Zhenming Wang, and Edward W. Woolery

Report of Investigations 14 Series XII, 2006

Contents

Figures

Tables

Our Mission

Our mission is to increase knowledge and understanding of the mineral, energy, and water resources, geologic hazards, and geology of Kentucky for the benefit of the Commonwealth and Nation.

Earth Resources—Our Common Wealth

www.uky.edu/kgs

Source Scaling, Subevent Distributions, and Ground-Motion Simulation in the Composite Source Model

Baoping Shi[1], Zhenming Wang[1], and Edward W. Woolery[2]

Abstract

Predicting strong ground motion from a large earthquake depends to a large extent on the development of a realistic source model. Strong ground motion was simulated using the composite source model. For comparison purposes, two different approaches were implemented in the source procedure simulation. For the first approach, the source was taken as a superposition of circular subevents with a constant stress drop. The number of subevents and their radii followed fractal law distribution, specified as a spatial random field, and subevents were allowed to overlap. This resulted in the total area of the subevents being much greater than the area of the main event, in order to catch the total seismic moment conservation. For the second approach, the number of subevents and their characteristic dimensions still obeyed fractal law, but subevents were distributed randomly over the main fault and did not overlap. The total area of subevents equaled the area of the main fault. In the second approach, the subevent stress drop was left as a free parameter to be adjusted, so that the sum of the subevents' seismic moment equalled the seismic moment of the main event. Using these two approaches, broadband ground motion was predicted from scenario earthquakes. The numerical simulations from these two approaches gave us similar results in waveform, peak ground motions, and frequency contents.

The major purpose of these simulations was to address some recent criticism of the overlapping procedure (e.g., numerical implementation) used in the previous composite source model. The generally good agreement between simulated and observed ground motions from the M_w4.6 June 18, 2002, Darmstadt, Ind., earthquake and the M_w4.0 June 6, 2003, Bardwell, Ky., earthquake shown in this study indicates that the numerical techniques of the composite source model are capable of reproducing the main characteristics of ground motion, both in the near field and the far field, in the central United States.

[1]Kentucky Geological Survey, University of Kentucky
[2]Department of Earth and Environmental Sciences, University of Kentucky

Introduction

Estimation of ground motion in the central United States is not straightforward because of a scarcity of moderate to large earthquakes. Therefore, synthetic strong ground-motion simulation could be part of a useful way to provide additional information about the potential damage moderate or large earthquakes could cause. The most widely used simulation methods to generate synthetic ground motion for the central United States are the stochastic point-source simulations of high-frequency ground motions by Hanks and McGuire (1981), Boore (1983), and Boore and Atkinson (1987) and the stochastic finite source model, which considers the rupture propagation effect, by Beresnev and Atkinson (1997, 1998).

Because the stochastic source model lacks a physical process, such as source rupture, directivity effect, and wave propagation, it is limited in ground-motion modeling. In addition, the challenges of performance-based engineering will increasingly require that structures be modeled as complex, dynamic, nonlinear, multi-degree-of-freedom systems. This requires the entire time histories of strong ground motion with three input components. In recent investigations by Somerville and others (1991), Zeng and others (1994), and Saikia and Somerville (1997), a kinematic model combined with empirical or theoretical Green's function computational techniques has successfully predicted ground motion with a realistic appearance of waveform and frequency content. The composite source model has three important advantages over the pure stochastic source model. First, the slip pulse distributed on the fault inherits a stochastic property and obeys a given fractal law. Thus, the complex earthquake physical process could be partly simulated. Second, the wave propagation effect is considered by computing the theoretical Green's function based on the elastodynamics equation for a layered solid structure. Third, a multicomponent ground motion can be generated through a computation of wave propagation in a given layered crustal structure.

For strong-motion simulation, the composite source model developed by Zeng and others (1994) was described with superposition of circular subevents, which are randomly distributed on the main fault. Therefore, the subevents are allowed to overlap each other, and the total area of the subevents is much larger than the area of the main fault. As a result, multiple triggering of subevents is generally used in order to achieve seismic moment conservation (Tumarkin and others, 1994). The multiple triggering involved in the composite source modeling is the same technique used in the stochastic finite-source model in order to keep the moment conservation (Beresnev and Atkinson, 1997).

We have enhanced the composite source model and simplified the problem with squared subevent distributions (Hartzell and others, 1999; Burjanek and others, 2003). The number of subevents with characteristic dimension greater than R was proportional to R^{-2}. The subevents did not overlap each other, and the sum of their areas equaled the area of the main fault. Each subevent was allowed to slip only once at the arrival time of the rupture front. Using this approach to generate synthetic seismograms gave us results in waveform, peak ground motion, and frequency contents similar to the results of Zeng and others (1994). One of the major purposes of this paper was to address some recent criticism of the overlapping procedure (e.g., numerical implementation) used in the previous composite source model (Zeng and others, 1994). In addition, we will show that, for near-fault strong ground motion, the composite source model simulation can characterize the near-source directivity effect and S-wave radiation pattern properly, consistent with the theoretical consideration.

Composite Source Model Methodology

In the composite source model developed by Zeng and others (1994), the source descriptions are based on the following assumptions: (1) the number of circular subevents with radius R is specified by

$$dN/d(\ln R) = pR^{-D} \tag{1}$$

where D is the fractal dimension, N is the number of subevents, and p is a constant of proportionality; and (2) the seismic moment of a subevent with size R satisfies the scaling relation of $M_i = CR_i^3 \Delta\sigma$, where C=16/7 for a circular fault model, and $\Delta\sigma$ is a stress-drop constant, independent of the subevent radius. The constraint of seismic moment conservation means that

$$p = \frac{7M^t}{16\Delta\sigma} \frac{3-D}{R_{max}^{3-D} - R_{min}^{3-D}} \tag{2}$$

where M^t is the seismic moment of the main event, R_{max} is the largest subevent, and R_{min} is a purely numerical parameter defined by computational constraints. Thus, for a random distribution of subevents on the main fault, the requirement of seismic moment conservation implies that the total area of subevents is greater than the area of the main fault; furthermore, the overlap of subevents on the fault is required at the computational implementation level (Fig. 1a).

We enhanced the composite source model with squared subevent distributions (Fig. 1b) (Hartzell and others, 1999; Burjanek and others, 2003) in which the number of subevents with characteristic dimension

(a)

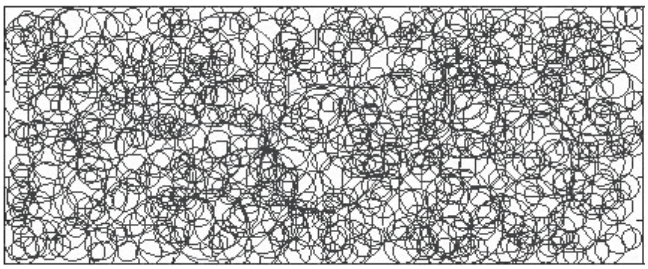

(b)

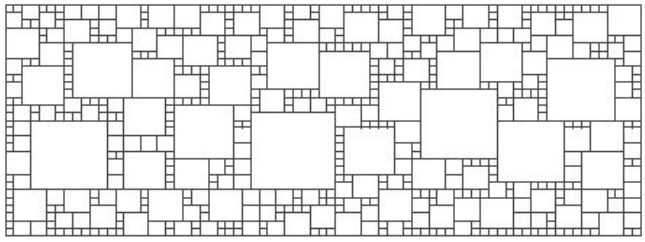

Figure 1. (a) Subevent (circular source model) distributions on the fault plane. From Zeng and others (1994). (b) Subevent (squared source model) distributions on the fault plane.

greater than R was proportional to R^{-2}; the subevents did not overlap each other, and the sum of their areas equaled the area of the main fault. In this case,

$$p = \frac{1}{\ln(\frac{R_{max}}{R_{min}})} \quad . \tag{3}$$

In equation (3), R_{max} and R_{min} are the largest and smallest subevents. Numerical generation of these size-dependent subevent distributions at the implementation level was discussed by Burjanek and others (2003). This approach allows each subevent to slip only once at the arrival time of the rupture front.

Seismic moment conservation requires that the total moment summed from subevents equals the moment of the main fault. Two approaches can reach this condition. First, with a given slip distribution function, we can assign the seismic moment for each subevent as

$$M_i = M^t / \sum_{i=1}^{N} S_i(R_i) \tag{4}$$

where $S_i(R)$ is the relative slip weight of the i^{th} subevent with size of R_i. Second, based on the source scaling relation of M (seismic moment) and $\Delta\sigma R^3$, $\Delta\sigma$ is a constant of proportionality related to the stress drop. The actual seismic moment is

$$M_o^R = \Delta\sigma \sum_{i=1}^{N} R_i^3 \tag{4}$$

We treated $\Delta\sigma$ as a free parameter to be adjusted in order to achieve the actual seismic moment $M_o^R = M^t$ (target total moment).

The source time function for each subevent was determined from its size as

$$\begin{cases} \dot{S}_i(t) = \Delta U_i (2\pi f_c^i)^2 \, t \exp(-2\pi f_c^i t) H(t) \\ f_c^i = K \dfrac{\beta}{R_i} \\ \Delta U_i = C \dfrac{\Delta\sigma}{\mu} R_i \end{cases} \tag{6}$$

where $\dot{S}(t)$ is the time derivative of source slip function, t is time after the subevent is triggered, $H(t)$ is the Heaviside step function, ΔU_i is mean slip of the i^{th} subevent, μ is the shear modulus, β is the shear-wave velocity, and C is a constant that depends on the geometry of the rupture. The corner frequency, f_c, has been related to the source characteristic dimension R_i of the i^{th} event. The value K depends on the rupture velocity and rise time, and is arbitrarily defined (Beresnev and Atkinson, 1997). For the Brune model, K conventionally equals 0.37 (Brune, 1970, 1971), and for the Haskell model (Aki and Richards, 1980), K conventionally equals 0.61.

The resulting ground-motion prediction is

$$U(t) = \sum_{i=1}^{N} \dot{S}_i(t) * G_i(t - t_i). \tag{3}$$

The rupture time, t_i, was determined using a constant rupture velocity of 2.8 km/s, corresponding to 85 percent of the shear-wave velocity, and $G_i(t)$ is a theoretical Green's function, denoting the ground displacement caused by a unit dislocation on the i^{th} subfault.

For the Green's function synthetic computation, a generalized reflection and transmission coefficient matrix method developed by Luco and Apsel (1983) and coded by Zeng and Anderson (1995) was used to compute elastic wave propagation in a layered elastic half-space in frequency/wavenumber domain. The generalized reflection and transmission coefficient matrix method is advantageous in the synthetic seismogram computation because it is based on solving the elastodynamic equation complying with the boundary conditions of the free surface, bonded motion at infinity, and continuity of the wave field across each interface.

In the implementation level, two specific schemes have been used to describe self-similar slip distributions related to the subevent distributions. For a blind prediction, the subevents were placed randomly within the fault plane shown in Figure 1b, and the resultant final slip distribution on the fault is shown in Figure 2a. For a specific source model (slip distributions are known on the fault), we adjusted the subevent distributions on the fault through a numerical manipulation to catch source slip information (Fig. 2b). In this case, the derived source

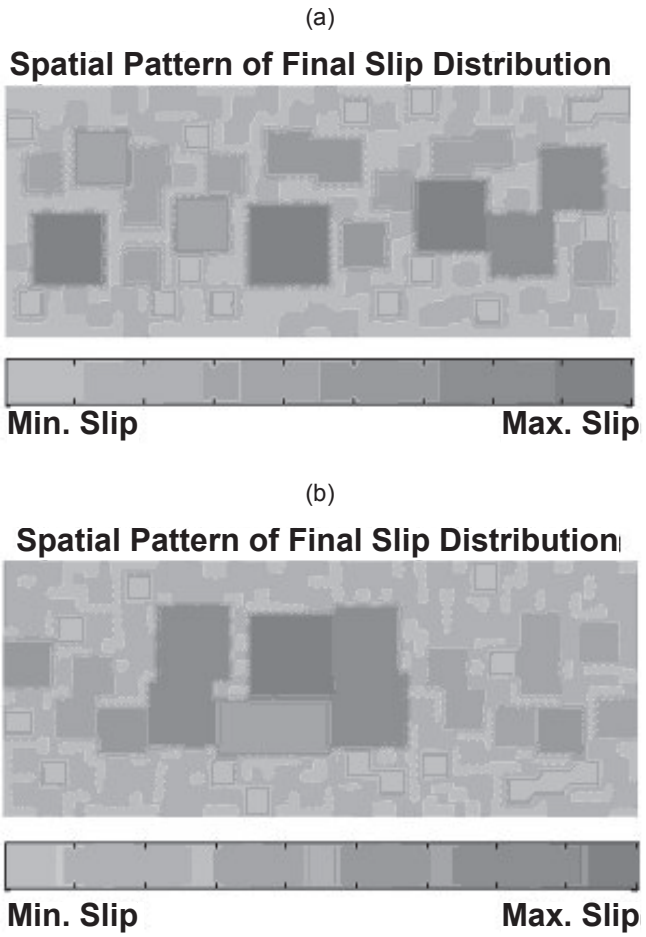

Figure 2. (a) Randomly generated nonuniform slip distributions based on the fractal composite source model. (b) A specific slip distribution pattern generated through numerical manipulation based on the fractal composite source model. In both cases, the slip distributions resemble the self-similar slip distributions proposed by Herrero and Bernard (1994).

parameters, such as slip and slip rate, and stress drop, were then used to simulate near-fault strong ground motions. In areas with very sparse local coverage, this approach provides strong ground-motion estimates that include the influences of earthquake-specific source finiteness and rupture directivity.

Simulation Results

We began with a simulation of a scenario earthquake with an M_w7.7 strike-slip fault located in the New Madrid Seismic Zone, with an emphasis on the near-fault effects. Figure 3a shows the fault geometry and site locations on the ground, and Figure 3b shows S-wave and P-wave radiation patterns around the fault. The moment magnitude was used to scale the fault model dimension using the relations of Somerville and others (2001); the derived input parameters from this relation are listed in Table 1. The velocity/density model developed by the U.S. Geological Survey (Frankel and others, 1996) was used in this simulation.

Source Effects

In the composite source model (Zeng and others, 1994), the size- and shape-dependent subevent distribution on the main fault plays an important role in defining the source rupture compelx. For comparison purposes, two types of composite source models were used in these simulations. We denoted the circular subevent source model as model-1 and the squared subevent source model as model-2. We generated size-dependent subevent distributions for both models according to equations (1), (2), and (3). Figure 4 shows the number of subevents versus subevent size distributions for both models. The total number of subevents for model-1 and model-2 were 680 and 641, respectively. In model-1, the number of subevents with size less than 2 km was 478, which is about 70 percent of the total number of subevents; there were two largest-size subevents, with a size of 9 km. In model-2, the number of subevents with size less than 2 km was 469, which is about 73 percent of the total number of subevents; there were two largest-size subevents, with a size of 9 km. Figures 4a and 4b clearly show that these two models have similar size-dependent subevent distributions, which were randomly distributed on the main fault, as shown in Figure 1. The total area of subevents from model-1 was 9,604.3 km^2, which is about 4.27 times the area of the main fault (2,250 km^2). Therefore, from the numerical implementation point of view, subevents are required to overlap with each other. The apparent stress drop, $\Delta\sigma$, from equation (5) for model-1 is 107.5 bars, and for model-2 is 126.6 bars, after adjustment (Zeng and others, 1994).

Source time functions used in equation (6) were K=0.3724 (Brune, 1970, 971), C=16/7π, μ=3 x 10^{11} dyne/cm^2, β=3 km/s=3 x 10^5 cm/s, and $\Delta\sigma$=107 bars=1.07 x 10^8 dyne/cm^2 and $\Delta\sigma$=126 bar=1.26 x 10^8 dyne/cm^2

Table 1. Input parameters for ground-motion simulation.

Parameter	*Range of Values*
Magnitude (M_w)	7.7
Fault mechanism	Strike-slip
Crust structure	USGS model[1] (α, β, ρ, Q, h)
Hypocenter	15 km
Fault length and width[2]	75 km and 30 km
Subevent dimension[2]	9 km (largest) and 1 km (smallest)
Slip function	Brune's pulse (Brune, 1970, 1971)
Rupture velocity	2.8 km/s
Fractal dimension	D=2
Stress drop	150 bars

[1]Frankel and others (1996)
[2]Somerville and others (2001)

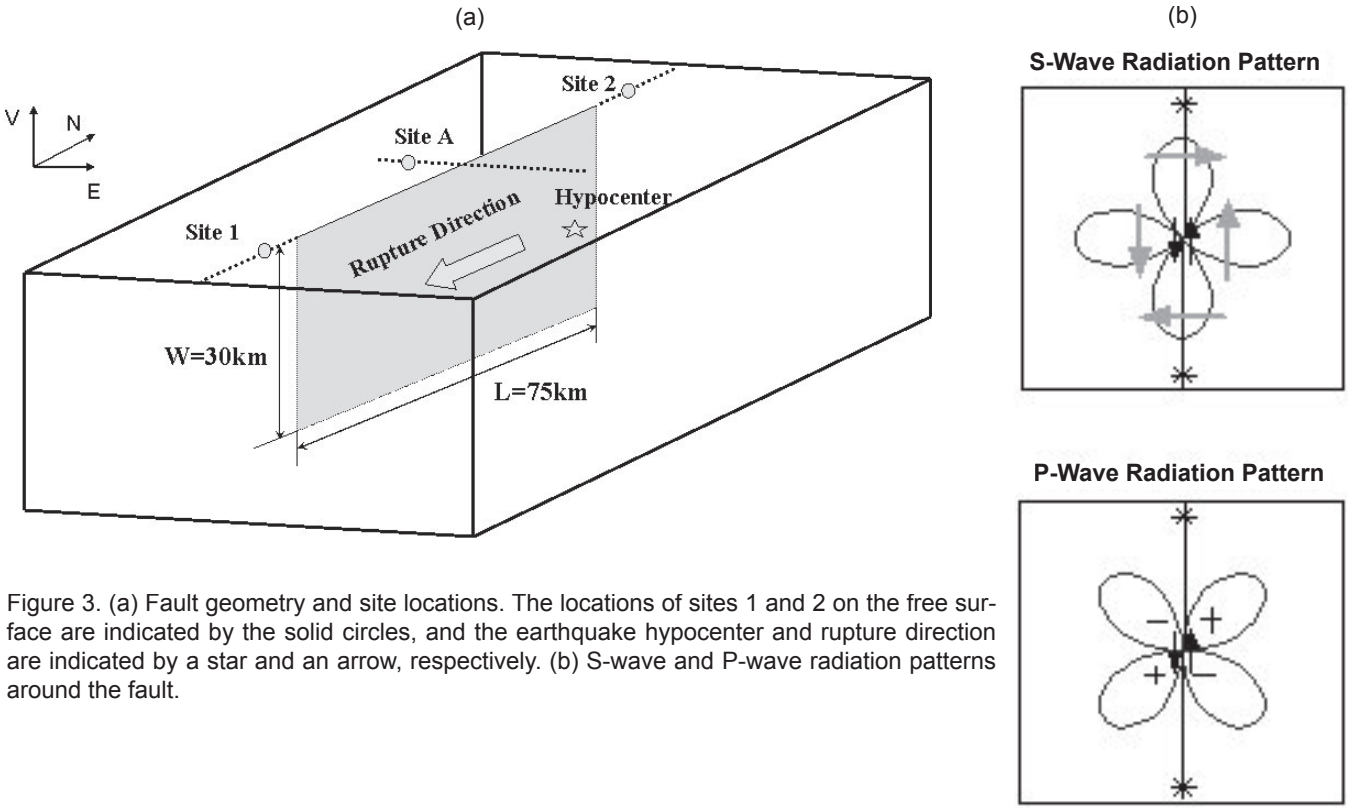

Figure 3. (a) Fault geometry and site locations. The locations of sites 1 and 2 on the free surface are indicated by the solid circles, and the earthquake hypocenter and rupture direction are indicated by a star and an arrow, respectively. (b) S-wave and P-wave radiation patterns around the fault.

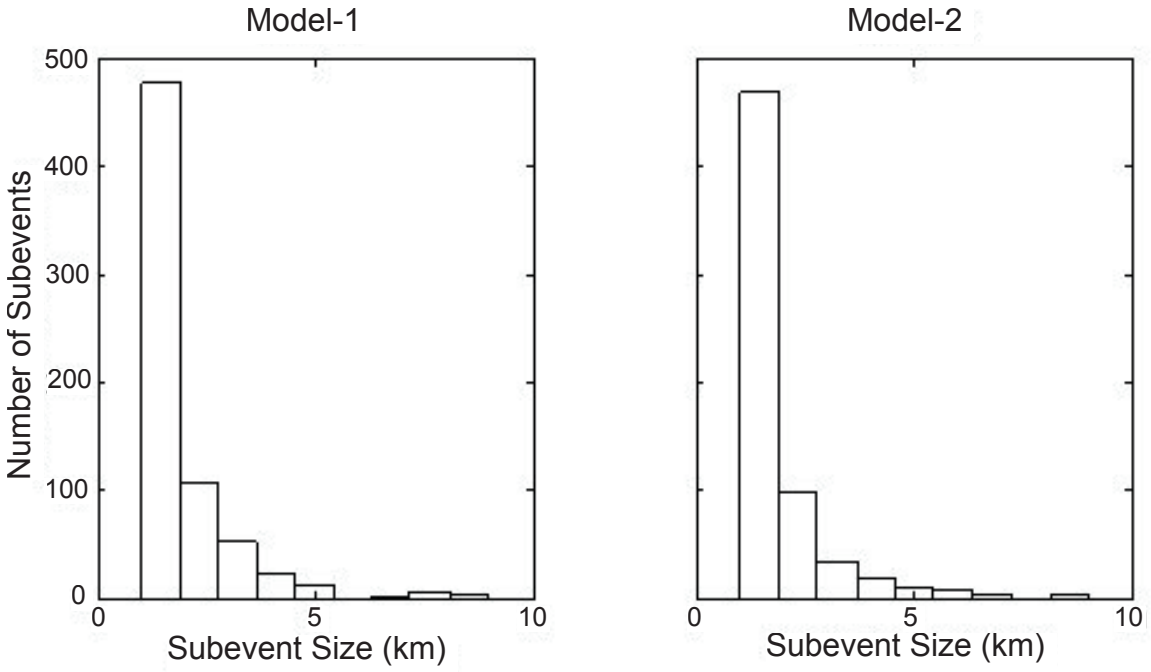

Figure 4. Fractal distribution of a number of subevents with respect to the characteristic dimension (subevent size). Typical size-dependent distributions derived from the circular source model (model-1) and squared source model (model-2) are shown.

for model-1 and model-2, respectively. The hypocenter and rupture direction are indicated by the star and arrow in Figure 3a, respectively. Figure 5 shows a simulated acceleration time series at site A; the shortest distance was 30 km from the main fault. The synthetic seismograms in Figures 5a and 5b were generated by source model-1 and source model-2, respectively. In both models, the duration and shape of the acceleration histories were predicted closely, and the fault-parallel components had larger peak values than those of other components, consistent with the S-wave radiation pattern near the fault (depicted in Figure 3b). The PGA values in both models were very similar for the fault-parallel component, and there were certain differences for the fault-normal and vertical components. These differences were mostly caused by different subevent distribution patterns in which the subevents were randomly assigned on the fault plane. In fact, each subevent assigned on the fault was specified as a point in which a slip pulse in equation (6) was radiated away from this point. Therefore, if the subevent distribution patterns are the same for both models, the resultant ground motions were the same too. Fault-parallel acceleration and displacement spectra for both models are compared in Figure 6. The agreement between these two models is remarkable, both in the low and high frequencies.

Near-Source Effect

In contrast to the far-field ground motions, which are typically stochastic processes having relatively longer duration, near-source ground motions are characterized by a relatively simple long-period pulse of strong motion having a relatively shorter duration. Long-period pulses of strong motions have been observed in recent large earthquakes, such as those at Landers in 1992, Northridge in 1994, Kobe in 1995, and Chi-Chi in 1999. These pulses are strongly influenced by the orientation of the fault, the direction of slip on the fault, and the sites' locations relative to the fault, which is termed the directivity effect due to the rupture propagation toward the site. Rupture directivity usually causes a large long-period pulse in the direction normal to

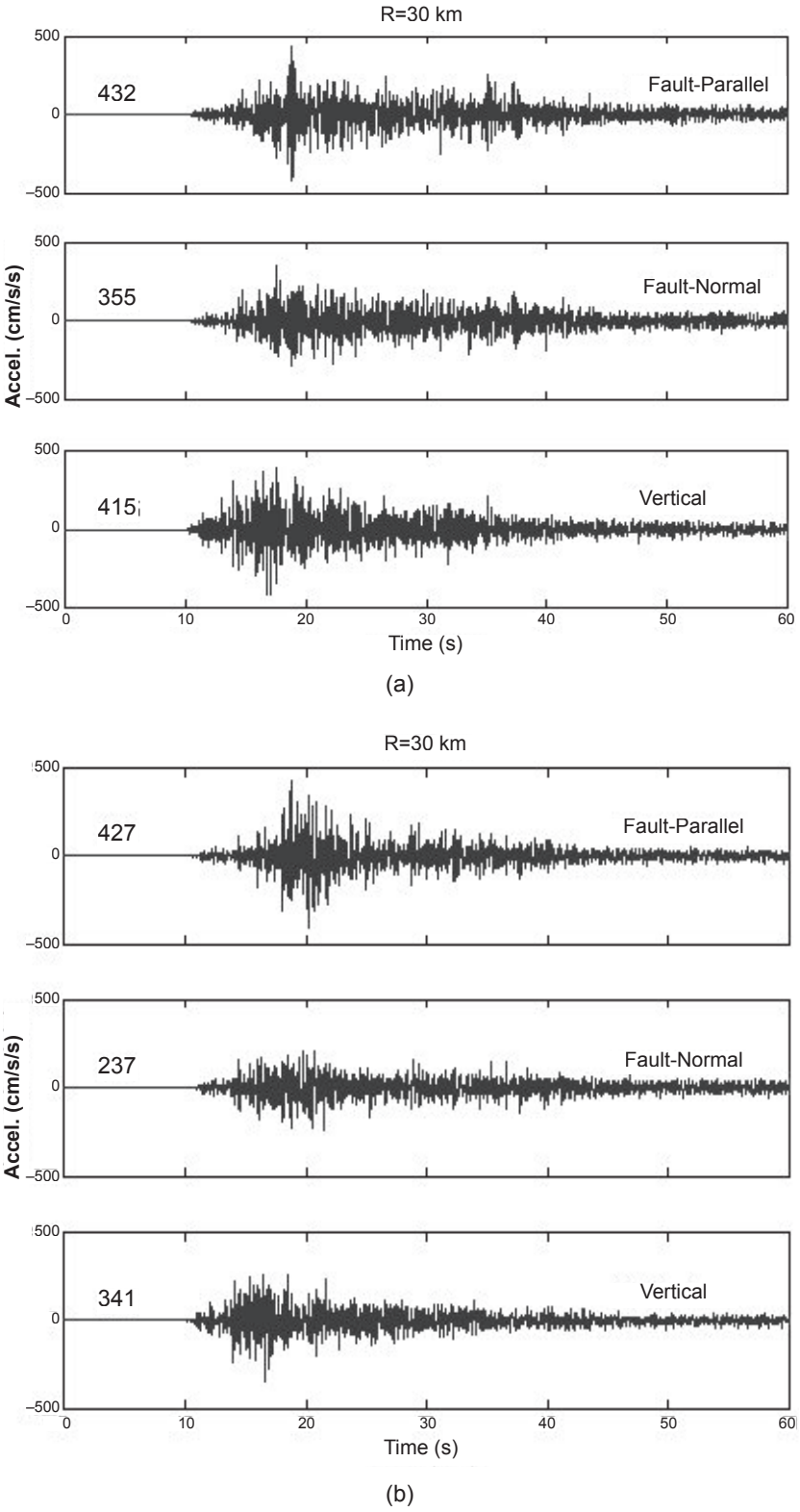

Figure 5. (a) Synthetic ground accelerations from model-1 (circular source model) with a distance of 30 km (site A). (b) Synthetic ground accelerations from model-2 (squared source model) with a distance of 30 km (site A).

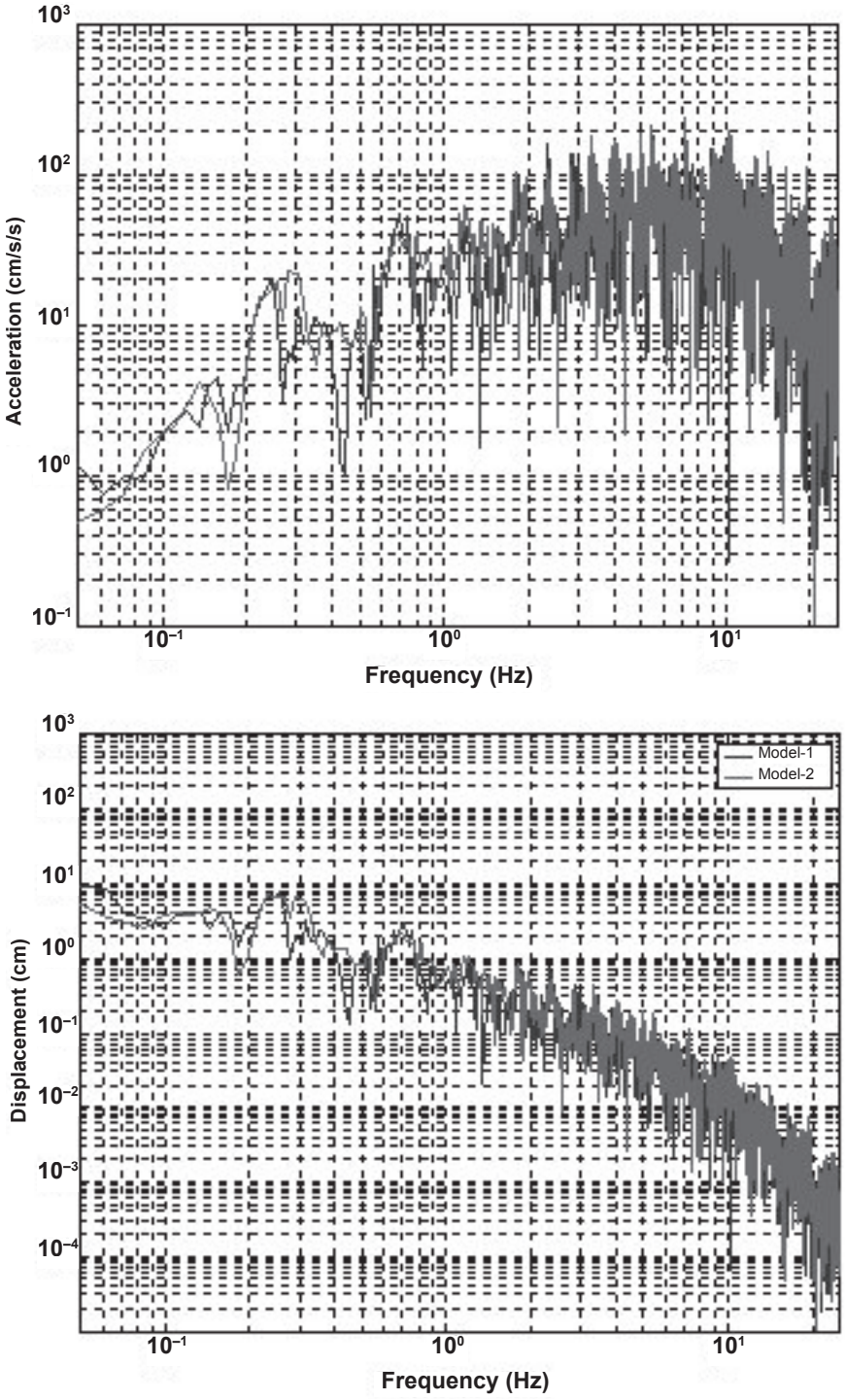

Figure 6. Fault-parallel acceleration and displacement spectra for model-1 (top) and model-2 (bottom). Both results are derived from Figure 5.

the fault. The conditions required for the generation of this pulse are met when the direction of the SH radiation pattern is maximum in the slip direction and the direction of rupture propagation coincides. In contrast, the SV radiation is at a minimum in the direction along the strike, resulting in a smaller ground motion parallel to the fault. To demonstrate the capability of near-source ground-motion simulation by the composite source model, we generated the ground-motion time histories at sites 1 and 2 (both at the right side of the fault line depicted in Figure 3b), in which the nearest distance to the fault was 10 km for both sites. The rupture starts at the fault surface near site 2 (hypocenter) and propagates toward site 1. The resultant ground motions at sites 1 and 2 are shown in Figure 7. The waveforms of the ground-motion time histories at site 1 (Fig. 7b) are larger and have sharper amplitudes for ground accelerations, velocities, and displacements, and are of shorter duration than those from site 2 (Fig. 7a). In other words, positive superposition of strong motion from each subevent generates stronger motion in the rupture direction. This phenomenon is called directivity effect. In addition, the systematic S-wave polarization and radiation patterns are clearly shown by the waveform components; the strike-normal components have much larger amplitude, consistent with the theoretical S-wave radiation pattern illustratated in Figure 3b.

PGA Comparison with Recent Attenuation Curves

Figure 8 statistically simulates ground motions from 5 km to 600 km and compares the peak horizontal accelerations with the attenuation relationships given by Atkinson and Boore (1995), Frankel and others (1996), Toro and others (1997), Somerville and others (2001), and Campbell (2003). The peak ground accelerations in these simulations are much lower than those derived from attenuation relationships at close distances (less than 20 km) by Atkinson and Boore (1995), Frankel and others (1996), and Toro and others (1997). The simulated PGA is very similar to that predicted from the attenuation relationships at close distances (less than 20 km) by Somerville and others (2001) and Campbell (2003). At far distances (greater than 50 km), the simulated peak ground accelerations are quite consistent with those predicted from the attenuation relationship of Somerville and others (2001).

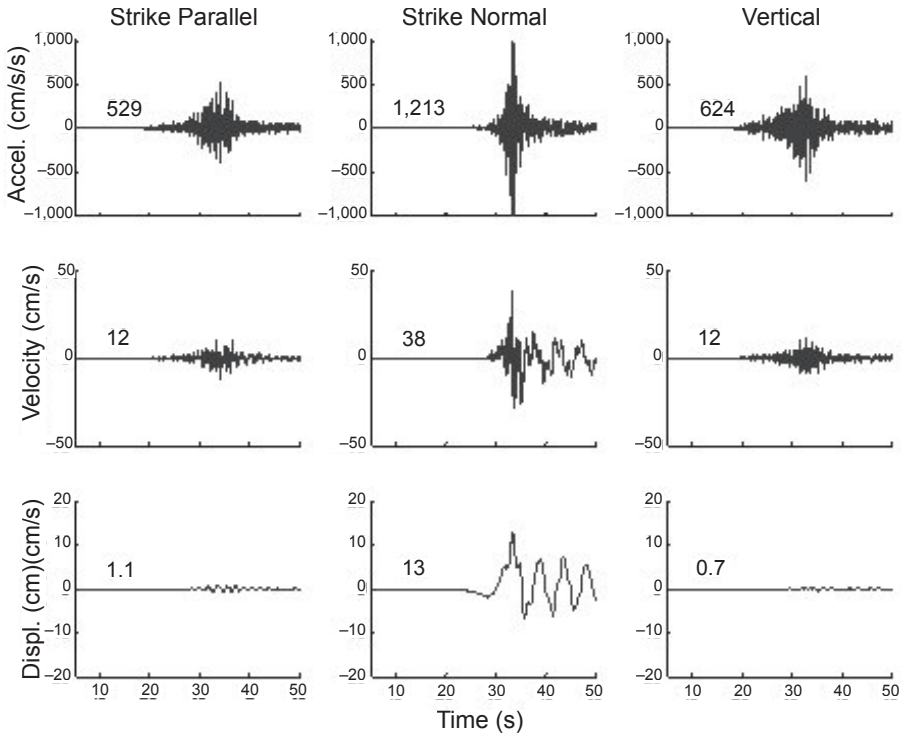

(a)

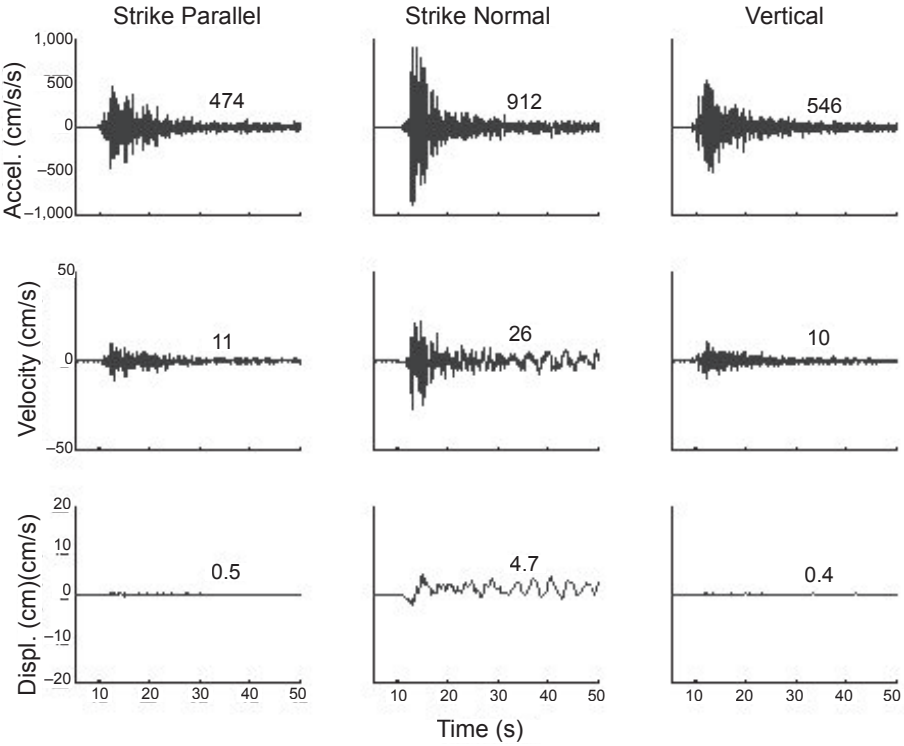

(b)

Figure 7. Synthetic ground-motion time histories at sites 1 (a) and 2 (b) of Figure 3a.

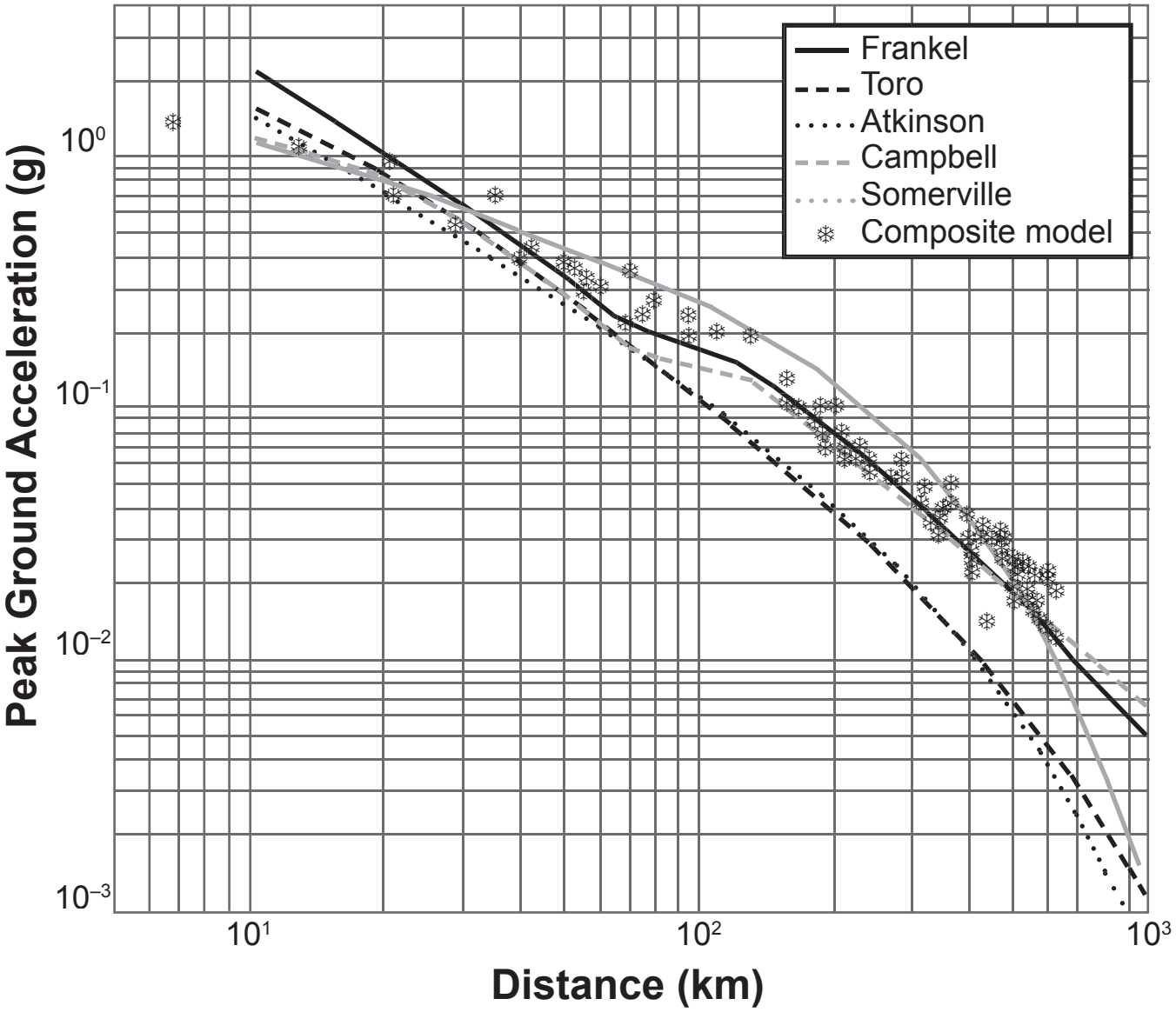

Figure 8. Comparison of synthetic peak horizontal acceleration values from an M_W=7.7 earthquake with the attenuation relations of Frankel and others (1996), Toro and others (1997), Atkinson and Boore (1995), Campbell (2003), and Somerville and others (2001).

Comparison with Observation

The time history simulations were compared to two observed earthquakes. The Darmstadt, Ind., earthquake occurred at 17.37 (UTC) on June 18, 2002, about 20 km west of Evansville. The focal mechanism solution indicates dipping strike-slip faulting (Kim, 2003); the source parameters for this event derived from teleseismic analysis (Kim, 2003) are summarized in Table 2. Eight strong-motion stations operated by the University of Kentucky and the U.S. Army Corps of Engineers, at epicentral distances ranging from 30 to 250 km, recorded the earthquake, as shown in Figure 9. The Bardwell earthquake occurred at 12.29 (UTC) on June 6, 2003, about 8 km south of Blandville, Ky. (Fig. 9). The focal mechanism solution indicates dipping strike-slip faulting with a west–east trend, as delineated by aftershock locations (Horton and Withers, 2003); the source parameters for this event derived from broadband seismic waveform analysis are summarized in Table 3. Three strong-motion stations at epicentral distances ranging from 14 to 67 km (WIKY, COKY, and VSAB on Figure 9) were triggered. Strong-motion records from these two earthquakes provide high-quality data for source study in the central United States. To include local site effects, a local velocity structure of surface soil layers derived from shallow reflection and refrac-

Table 2. Source parameters of the June 18, 2002, Darmstadt, Ind., earthquake and the June 6, 2003, Bardwell, Ky., earthquake.

Date	17.37 (UTC), June 18, 2002	12.29 (UTC), June 6, 2003
Epicentral Location	38.9N/89.9E	38.9N/89.9E
Moment Magnitude	4.6	4.02
Seismic Moment (dyne-cm)	3.52×10^{23}	1.202×10^{22}
Depth (km)	18±2	2.5±0.5
Strike	176°	76°
Dip	86°	76°
Rake	10°	5°

tion data (Street and others, 1995) was also used in the Green's function calculation. Table 4 lists the layered soil structures used in this study.

Darmstadt, Ind., Earthquake. Several key parameters of the source model used for the simulations were obtained by repeat trial and by examining the resultant seismograms at the J.T. Myers and Newburgh stations. Figures 10 and 11 show the synthetic seismograms and observed data recorded in the stations at pier 6 of J.T. Myers Lock and Dam and pier 9 of Newburgh Lock and Dam, with epicentral distances of 30 and 35 km, respectively. In each figure, the right column shows three components of acceleration and velocity time histories, and the left column gives corresponding synthetic results. The appearance of the waveform, duration, and frequency

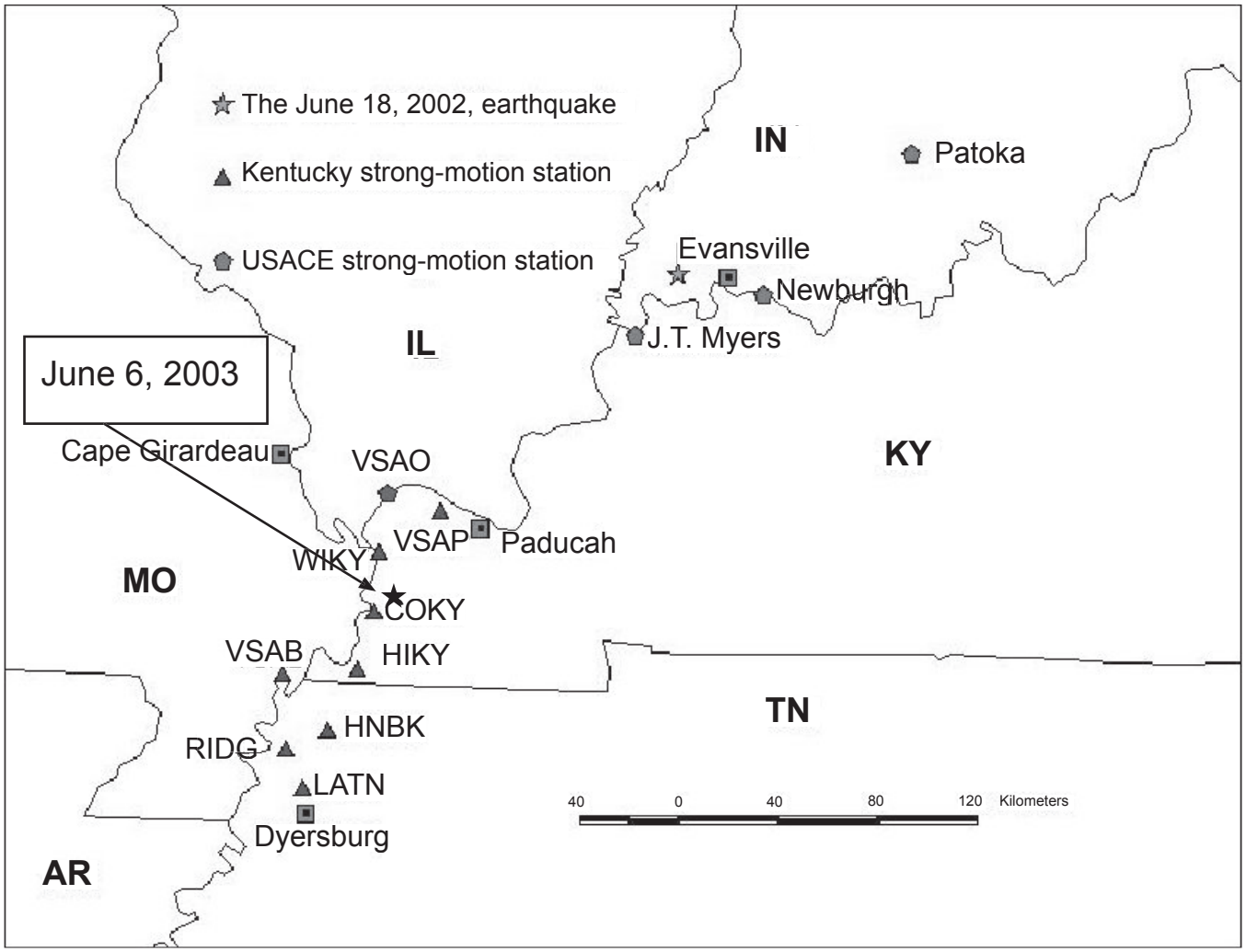

Figure 9. Locations of the strong-motion stations and the epicenters of the June 18, 2002, Darmstadt, Ind., earthquake and the June 6, 2003, Bardwell, Ky., earthquake.

Table 3. Parameters of the composite source model used to model M_w4.6 and M_w4.0 earthquakes.

Parameter	*Value*	
	Darmstadt Earthquake	*Bardwell Earthquake*
L (fault length along the strike)	2.5 km	1.0 km
W (rupture width)	2.0 km	1.0 km
M_o (seismic moment)	3.52 x 10^{23} dyne/cm	1.2 x 10^{22} dyne/cm
R_{max} (largest subevent radius)	0.5–0.75 km	0.25–0.5 km
$\Delta\sigma$ (subevent stress drop)	150 bars	150 bars
V_r (rupture velocity)	2.8 km/s	2.8 km/s
D (fractal dimension)	2.0	2.0

Table 4. Soil model used at WIKY, COKY, VSAB, J.T. Myers, and Newburgh strong-motion stations.

Thickness (m)	*V_p (m/s)*	*Q_p*	*V_s (m/s)*	*Q_s*	*Density (gm/cm^3)*
5	200	30	150	20	1.5
6.5	300	50	200	30	1.8
100	600	80	400	50	2.0

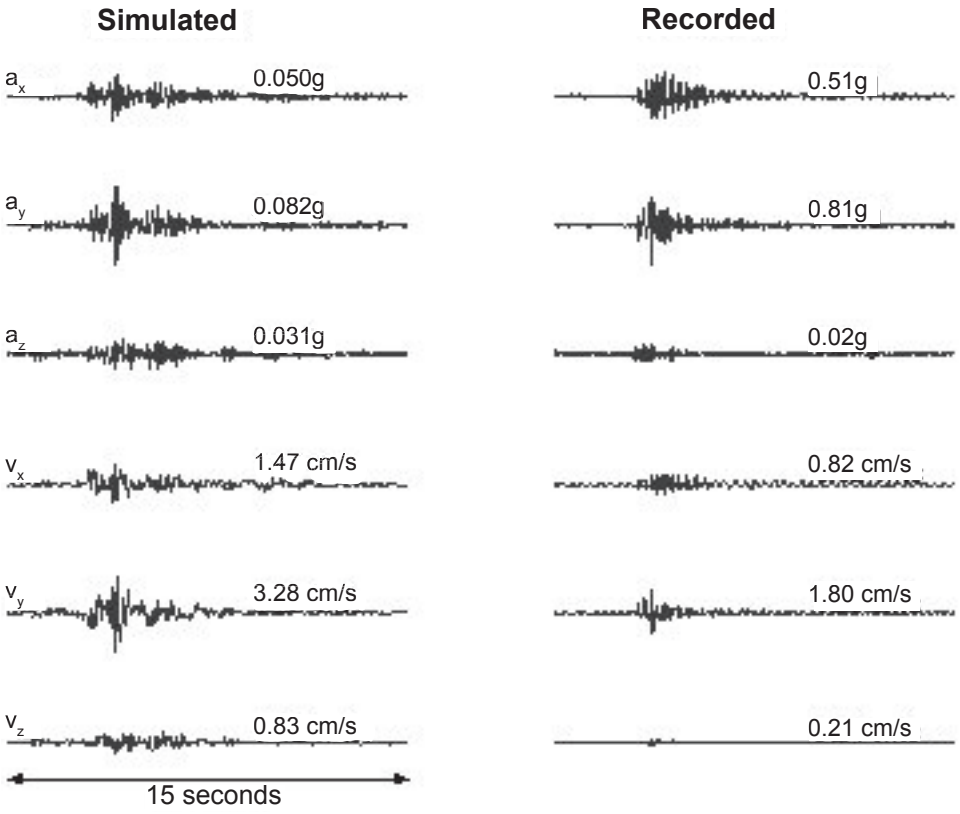

Figure 10. Comparison of observed and synthetic ground motions at J.T. Myers station. Observed acceleration and velocity are in the right column. The horizontal components a_x and a_y refer to the instrument orientations, and the vertical component is denoted by a_z.

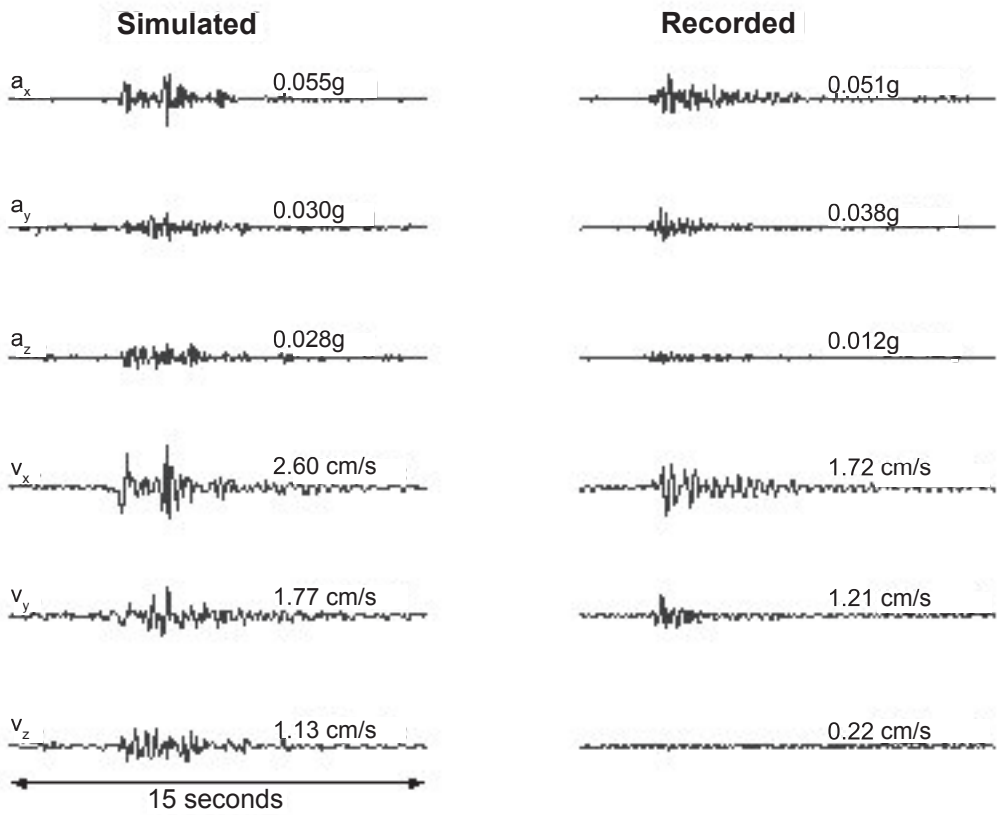

Figure 11. Comparison of observed and synthetic ground motions at Newburgh station. Observed acceleration and velocity are in the right column. The horizontal components a_x and a_y refer to the instrument orientations, and the vertical component is denoted by a_z.

contents match well with the observations. At J.T. Myers, located directly in front of the rupture direction, the synthetic and recorded ground motions of acceleration and velocity have higher frequencies, and ground motion is higher. At Newburgh, a normal component of radiated seismic energy dominates the ground-motion patterns, which are indicated from the synthetic pulse-shaped acceleration and velocity waveforms. In these two examples, the synthetic results of peak values of particle accelerations and velocities are in good agreement with the observations (Figs. 10–11). There are prominent pulses in the horizontal components in the particle acceleration and velocity, with frequency content comparable to the observations. Some of the differences between the synthetics and observations could come from the lack of information about the earthquake dynamic rupture process or soil/structure interactions. The size of the largest subevents, rupture directions, regional velocity model, and local soil structure also contributed to some of the uncertainty. In addition, the focal mechanism cannot be determined precisely because of the small fault size. In fact, to match the waveform precisely in phase, peak value, and duration, an inversion technique based on the genetic algorithm was used in composite source modeling for a recent source complex study (Zeng and Anderson, 1996; Anderson and others, 2001). This approach gives us insight into the fault rupture and slip patterns distributed in a fault with a complex slip pattern. For the central United States, because of the lack of significant earthquake records, a trial-and-error test could be a more practical way to produce the synthetic seismogram. For the remaining stations, such as COKY, HIKY, and RIDG, since the corresponding epicentral distances are greater than 100 km, the peak values of the synthetic ground motions are slightly smaller than observed peak values, but frequency contents and duration are comparable between the synthetic and recorded data.

Bardwell Earthquake. The June 6, 2003, Bardwell, Ky., earthquake was a slight event with a moment magnitude of 4.0. The most recent focal-mechanism solution

indicated that the earthquake was caused by strike-slip faulting occurring about 2.5 km beneath the surface. Three strong-motion stations (WIKY, COKY, and VSAB) operated by the University of Kentucky were triggered by this earthquake. The distances of these stations from the epicenter are about 14 km (WIKY), 16.5 km (COKY), and 64 km (VSAB). Using source scaling law (Somerville and others, 2001), we constructed a composite source model to simulate ground motions of this event, and the synthetic time histories were compared with recorded seismograms from the stations. Figures 12a–c illustrate the synthetic and observed acceleration time histories for WIKY, COKY, and VSAB, respectively. These plots clearly show that the waveforms of the synthetic time histories are very similar to waveforms of the observations; the peak value of accelerations, duration, and frequency content from the synthetics also matched well with the observations.

Conclusions

The recently developed composite source model, combined with a theoretical Green's function calculation, has the flexibility of incorporating source complexities, the wave propagation effect, and local site effects into strong-motion simulation. Some argue that the largest ruptures could overwhelm the effects of the modeled rupture front, effectively washing out any directivity effect, so that the composite source model may not correctly simulate near-fault effects. This is not quite true in the case of near-fault ground motion, especially that caused by the source directivity effect. Fractal subevent distributions play a significant role in modeling source complexes (by eliminating amplitude deficiencies at the mid-frequency spectrum). Synthetic ground motions, both from the circular source model (overlap allowed) and the squared source model (overlap not allowed), give similar results in wave form, peak ground motions, durations of ground motion, and frequency contents. Therefore, although the overlap assumption with a Brune's circular model (Zeng and others, 1994) is required from a moment conservation consideration (Tumarkin and others, 1994), it does not mean that the rupture process occurs more than once or that the fault plane radiates energy more than once, as argued by Beresnev and Atkinson (1997). Each subevent within the main fault acts as a source at a specific point on the main fault, from which seismic energy radiates and propagates to the ground. Ground motion is a contribution from such points on the main fault. Thus, in the numerical implementation level, whether overlap occurs (circular source model) or does not occur (squared source model) does not mean that any physical rupture processes, such as a radical rupture process for a circular dislocation, have been involved in the simulation of dynamic rupture. In fact, the overlapped or not-overlapped subevent distributions on the main fault merely imply possible heterogeneous slip distributions on the main fault, which is usually assumed in a kinematic source model.

The assumption of constant stress drop over the fault plane leads to robust synthetics that are not sensitive to the distribution pattern of size-dependent subevents or slip on the fault. In this case, each size-dependent subevent has the same peak value of slip rate, and the sharpness of the slip rate, derived from equation (6), is controlled by f_c, the corner frequency. For a traditional dislocation model, the particle velocity and acceleration are proportional to $\Delta\sigma$, the stress drop in the vicinity of the fault, as discussed by Brune (1970). Since the number of subevents with size less than 2 km is about 70 percent of the total number of subevents, our numerical analysis has shown that the radiated seismic energy from the subevents with size less than 2 km is about 71 percent of the total seismic energy radiated from the main event, and less than 5 percent of the seismic energy is contributed from the largest subevents (9 km); this also implies that small subevents dominate the seismic energy radiation. Therefore, the near-fault ground motion characterized by strong directivity effect (seismic energy-focusing), systemaic S-wave polarization, and radiation pattern could be reproduced from the composite source model.

We systematically compared the composite source model synthetics with the strong-motion recordings of the M_w4.6, June 18, 2002, Darmstadt, Ind., earthquake and the M_w4.02, June 6, 2003, Bardwell, Ky., earthquake. The synthetic seismograms from the composite source model demonstrated that this approach produces very realistic ground motions, with statistical properties consistent with the observations in the near-source sites. Compared with other stochastic source models, the composite source model gives more useful information about source physical processes and wave propagation effects, which reflect a range of stress drops among the subevents, R_{max} (the largest radius of a subevent), and rupture directivity. A weakness of the composite source model is that the stress drop, $\Delta\sigma$, and R_{max}, the largest radius of the subevent, are specified by trial-and-error modeling. Recent studies by Zeng and Anderson (1996) and Anderson and others (2001) addressed this problem by developing a genetic inversion algorithm that finds an optimum distribution and size of subevent in order to model synthetic seismograms. Combined with a genetic algorithm developed by Zeng and Anderson (1996), a composite source model could match the observed seismogram, both in phase and amplitude.

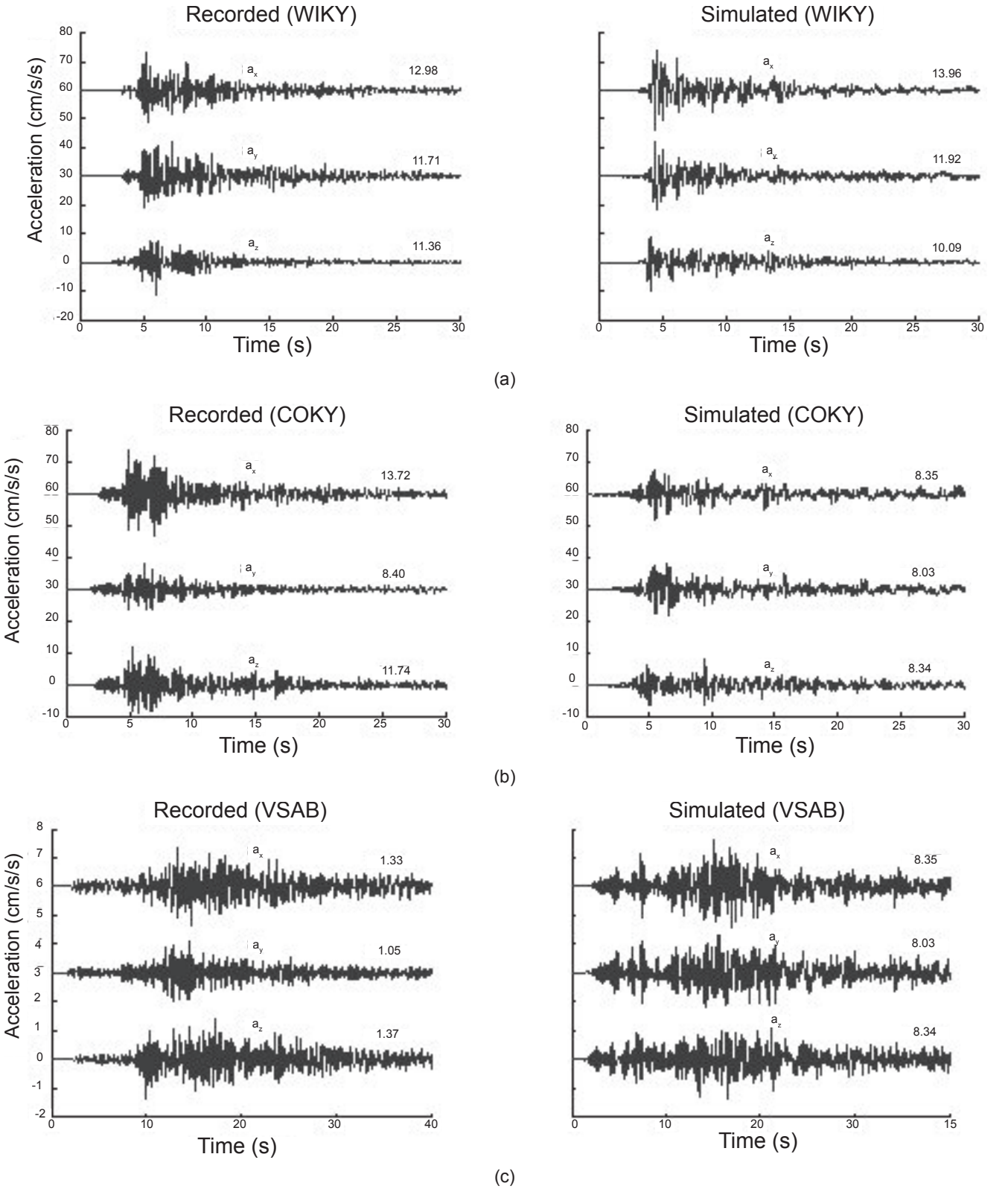

Figure 12. Comparison of observed and synthetic ground motions at stations WIKY (a), COKY (b), and VSAB (c). Observed acceleration and velocity are in the right column. The horizontal components a_x and a_y refer to the instrument orientations, and the vertical component is denoted by a_z.

References Cited

Aki, K., and Richards, P.G., 1980, Quantitative seismology: Theory and methods: New York, W.H. Freeman and Co., 932 p.

Anderson, J.G., Zeng, Y., and Sucuoglu, H., 2001, Analysis of accelerations from the 1 October 1995 Dinar, Turkey, earthquake: Bulletin of the Seismological Society of America, v. 91, p. 1433–1445.

Atkinson, G.M., and Boore, D.M., 1995, Ground motion relations for eastern North America: Bulletin of the Seismological Society of America, v. 85, p. 17–30.

Beresnev, I.A., and Atkinson, G.M., 1997, Modeling finite-fault radiation from ωn spectrum: Bulletin of the Seismological Society of America, v. 87, p. 67–84.

Beresnev, I.A., and Atkinson, G.M., 1998, FINSIM—A FORTRAN program for simulating stochastic acceleration time histories from finite faults: Seismological Research Letters, v. 69, p. 27–32.

Boore, D.M., 1983, Stochastic simulation of high-frequency ground motion based on seismological models of the radiated spectra: Bulletin of the Seismological Society of America, v. 73, p. 1865–1894.

Boore, D.M., and Atkinson, G.M., 1987, Stochastic prediction of ground motion and spectral response parameters at hard-rock sites in eastern North America: Bulletin of the Seismological Society of America, v. 77, p. 440–467.

Brune, J.N., 1970, Tectonic stress and spectra of seismic shear waves from earthquakes: Journal of Geophysical Research, v. 75, p. 4997–5009.

Brune, J.N., 1971, Correction. Tectonic stress and spectra of seismic shear waves from earthquakes: Journal of Geophysical Research, v. 76, p. 5002.

Burjanek, J., Irikura, K., and Zahradnik, J., 2003, Strong ground motion prediction by composite source model: Eos, v. 84, no. 46.

Campbell, K.W., 2003, Prediction of strong ground motion using the hybrid empirical method and its use in the development of ground-motion (attenuation) relations in eastern North America: Bulletin of the Seismological Society of America, v. 93, p. 1012–1033.

Frankel, A., Mueller, C., Barnhard, T., Perkins, D., Leyendecker, E.V., Dickman, N., Hanson, S., and Hopper M., 1996, National seismic hazard maps: Documentation, June 1996: U.S. Geological Survey Open-File Report 96-532, 110 p.

Hanks, T.C., and McGuire, R.K., 1981, The character of high frequency strong ground motion: Bulletin of the Seismological Society of America, v. 71, p. 2071–2095.

Hartzell, S., Harmsen, S., Frankel, A., and Larsen, S., 1999, Calculation of broadband time histories of ground motion: Comparison of methods and validation using strong ground motion from the 1994 Northridge earthquake: Bulletin of the Seismological Society of America, v. 89, p. 1484–1504.

Herrero, A., and Bernard, P., 1994, A kinematic self-similar rupture process for earthquakes: Bulletin of the Seismological Society of America, v. 84, p. 1216–1228.

Horton, S.P., and Withers, M., 2003, Aftershocks of the M_w=4.0 Bardwell, Ky., earthquake of June 6, 2003 [abs.]: Seismological Society of America, Eastern Section, Annual Meeting, Program and Abstracts, p. 20.

Kim, W., 2003, The 18 June 2002 Caborn, Indiana, earthquake: Reactivation of ancient rift in the Wabash Valley Fault Zone?: Bulletin of the Seismological Society of America, v. 93, p. 2201–2211.

Luco, J.E., and Apsel, R.J., 1983, On the Green's function for a layered half space: Bulletin of the Seismological Society of America, v. 73, p. 909–929.

Saikia, C.K., and Somerville, P.G., 1997, Simulated hard-rock motions in Saint Louis, Missouri, from large New Madrid earthquakes ($M_w \geq 6.5$): Bulletin of the Seismological Society of America, v. 87, p. 123–139.

Somerville, P., Collins, N., Abrahamson, N., Graves, R., and Saikia, C., 2001, Ground motion attenuation relations for the central and eastern United States: Final report to U.S. Geological Survey.

Somerville, P.G., Sen, M.K., and Cohee, B., 1991, Simulation of strong ground motions recorded during the 1985 Michoacan, Mexico, and Valparaiso, Chile, earthquakes: Bulletin of the Seismological Society of America, v. 81, p. 1–27.

Street, R.E., Woolery, E.W., Wang, Z., and Harris, J., 1995, Short note on shear-wave velocity and other site conditions at selected strong-motion stations in the New Madrid Seismic Zone: Seismological Research Letters, v. 66, p. 56–63.

Toro, G.W., Abrahamson, N.A., and Schneider, J.F., 1997, Model of strong ground motions from earthquakes in central and eastern North America: Best estimates and uncertainties: Seismological Research Letters, v. 68, p. 41–57.

Tumarkin, A.J., Archuleta, R.J., and Madariaga, R., 1994, Scaling relations for composite earthquake models: Bulletin of the Seismological Society of America, v. 84, p. 1279–1283.

Zeng, Y., and Anderson, J.G., 1995, A method for direct computation of the differential seismogram with respect to the velocity change in a layered elastic solid: Bulletin of the Seismological Society of America, v. 85, p. 300–307.

Zeng, Y., and Anderson, J.G., 1996, A composite source modeling of the 1994 Northridge earthquake using genetic algorithm: Bulletin of the Seismological Society of America, v. 86, p. 71–83.

Zeng, Y., Anderson, J.G., and Yu, G., 1994, A composite source model for computing realistic synthetic strong ground motions: Geophysical Research Letters, v. 21, p. 725–728.